Supplementary Information for

Speech can produce jet-like transport relevant to asymptomatic spreading of virus

Manouk Abkarian, Simon Mendez, Nan Xue, Fan Yang & Howard A. Stone

Howard A. Stone.
E-mail: hastone@princeton.edu

This PDF file includes:

Supplementary text
Figs. S1 to S4
Table S1
Legends for Movies S1 to S5
SI References

Other supplementary materials for this manuscript include the following:

Movies S1 to S5

Supporting Information Text

Methods: Numerical Simulations

Physics.

Physical Model. Three-dimensional numerical simulations are performed in an idealized situation of non-buoyant jets, where temperature effects are neglected. The gas flows in a low-Mach regime where compressibility effects are negligible. To account for turbulence, we use Large Eddy Simulations (LES) (1), which allows solving the large scales of the flow while modelling the contributions of the unresolved small scales on the large scales. The unknowns are spatially filtered quantities. The fluid flow is thus represented by the incompressible versions of the filtered continuity and Navier-Stokes equations:

$$\frac{\partial \bar{u}_i}{\partial x_i} = 0, \qquad [1]$$

$$\rho \frac{\partial \bar{u}_i}{\partial t} + \rho \frac{\partial \bar{u}_i \bar{u}_j}{\partial x_j} = -\frac{\partial \bar{p}}{\partial x_i} + \mu \frac{\partial^2 \bar{u}_i}{\partial x_j \partial x_j} + \frac{\partial \tau_{ij}}{\partial x_j}, \qquad [2]$$

where $\bar{u}_i$ is the filtered fluid velocity component in the ith direction, $\bar{p}$ the filtered pressure, t the time, x_i the spatial coordinate in the ith direction, ρ the constant density and μ the constant dynamic viscosity. $\tau_{ij} = \rho(\overline{u_i u_j} - \bar{u}_i \bar{u}_j)$ is the residual stress-tensor coming from the subgrid-scale unresolved contribution, for which a closure needs to be provided. Here we use the so-called sigma model (2) which has notably been built to yield zero extra dissipation in laminar flows, so that it is well adapted to situations at moderate Reynolds numbers where transition to turbulence occurs (3, 4), which is the case here. The fluid considered is assumed to represent air at constant ambient temperature. The kinematic viscosity is fixed at $\nu = \mu/\rho = 1.5 \times 10^{-5}$ m^2/s.

Lagrangian tracers are used in the simulations to visualize the development of the jet. They are massless particles convected at the local velocity of the flow. The position X_i of each tracer evolves in time as

$$\frac{\partial X_i(t)}{\partial t} = \bar{u}_i(X_i, t). \qquad [3]$$

Computational Domain. A 2D slice of the computational domain is displayed in Fig. S1. The computational domain is a sphere of diameter 3.0 m, in which a small sphere of diameter 15 cm is included to crudely represent a head. The head sphere center is located at $x = -0.075$ m, $y = z = 0$. The jet issues from a channel of fixed cross section, an ellipse of semi-axes $a_y = 0.01$ m and $a_z = 0.015$ m. The in-flow is located at the center of the sphere, 7.5 cm upstream of the mouth exit. The jet issues from the mouth exit at $x = 0$ and is directed towards the positive values of x. The center of the sphere of the computational domain (that of diameter 3 m) is located at $x = 0.825$ m, $y = z = 0$.

Boundary Conditions. The in-flow boundary condition located at $x = -0.075$ m is a uniform Dirichlet boundary condition imposed to obtain the flow rate signals displayed in Fig. 4 of the paper, for the cases with an exhaled volume of 0.5 L per breath (or cycle). The in-flow signals are split into an exhalation phase and an inhalation phase with different duration but identical volume exhaled and inhaled. Depending on the case, the signals may be multiplied by a factor of 1.5 or 2.0 to yield higher exhaled/inhaled volume per breath (0.75 L and 1.0 L per breath, respectively). The signal is perfectly periodic along time, with a period of 4.0 s for all cases. For all computed cases, the jets are initially in a laminar state and transition to turbulence naturally, notably due to the modulation of the flow. At the in-flow, Lagrangian tracers are injected randomly over the in-flow surface, with a fixed concentration along each simulation, the injection rate of tracers depending linearly on the gas flow rate. The concentration is adjusted so that about 65 000 tracers per cycle are injected in each case.

Boundary conditions on the head surface are impermeable non-slipping walls imposed as a zero velocity Dirichlet boundary condition. Finally, the far-field boundary condition is also a Dirichlet boundary condition on velocity, which varies along time in order to exactly ensure mass conservation in the domain. In practice, the ratio of surface area between the far-field boundary condition and the inlet is such that the velocity at the far field boundary condition is typically five orders of magnitude smaller than that in the jet.

Numerics.

Flow Solver. The flow solver YALES2BIO (3–5) is used in the present work (https://imag.umontpellier.fr/~yales2bio/). The fluid equations are discretized using a fourth-order finite-volume scheme, adapted to unstructured grids (6, 7). To solve the incompressible filtered equations, the projection method introduced by Chorin (8) and modified by Kim & Moin (9), based on the Helmholtz-Hodge decomposition, is used. The prediction step is advanced in time using a TFV4A 4th-order scheme in time, which combines a 4th-order Runge-Kutta scheme with a Lax-Wendroff-like scheme also of the 4th-order (10). The correction step involves a Poisson equation to calculate pressure. This equation is solved with the Deflated Preconditioned Conjugate Gradient algorithm (11).

The time step is fixed thanks to a classical Courant–Friedrichs–Lewy (CFL) condition which limits the convective time step. The CFL number is fixed to 0.9 in all simulations.

Regarding the advancement of the Lagrangian tracers, the fluid velocity is interpolated at the tracer location and a third-order Runge-Kutta scheme is used to advance Eq. 3.

Meshing. We use a tetrahedral mesh generated thanks to the open source meshing software Gmsh (https://gmsh.info) (12). It contains 17.7 million elements. Mesh resolution is 2 mm near the mouth and in the jet in the first 60 cm downstream of the mouth exit then smoothly increased. More rapid grid coarsening is employed to save computational resources downstream of $x = 1.65$ m. Mesh resolution in the far field is nowhere more than 3 cm (see Fig. S1). Some tests with a grid twice as fine in each direction (142 million elements) have been performed to verify the independence of the results on the grid level (see next section).

Simulations.

Simulations operating conditions. The simulations reported are all performed in the same computational domain, with the same numerics. The differences between the simulations lie in the flow rate at the mouth exit, with different volumes per breath (in and out) and different in-flow signals. Table S1 gathers the characteristics of the simulations presented in this study. Multicycle simulations and 1-cycle simulations are presented. Multicycle simulations have been run for several cycles imposing the flow rates of Fig. 4 of the main text in a periodic manner. They are denoted by B**, C**, P** ans S** depending on the signal used. P** ans S** denote speaking signals. They correspond to signals extracted from Subtelny et al. (1966) of people pronouncing 'Peter Piper picked a peck' (P) and 'Sing a song of six pence' (S). B** and C** are more characteristic of breathing, but with different ratios between exhalation and inhalation times (see Fig. 4). The numbers after the letter indicate the exhaled volume per breath. For the simulation of the 'Peter Piper picked a peck' sentence for instance, the simulation P50 uses the in-flow signal of Fig. 4C, with an exhaled volume per cycle of 0.5 L. Simulations at 0.75 L and 1.0 L per cycle are referred to as P75 and P100, and are obtained by multiplying the input flow rate signal of P50 by 1.5 and 2.0, respectively. Two 1-cycle simulations have been performed, 1P75 and 1S50. They use the same in-flow signals as P75 and S50 during the first cycle (first 4 seconds), then a zero in-flow during the rest of the simulations. Both the peak and the averaged Reynolds numbers are reported. The averaged value is calculated during the exhalation only.

Table S1 also reports some characteristics of the simulation results: the jet semi-angle α used in the non-dimensional results presented in the main text, the jet length after 1 cycle and the plume Reynolds number (the Reynolds number in the plume far from the inflow, at $x = 1$ m). Some comments about reproducibility are necessary before presenting results.

Reproducibility of the results and grid convergence. This study presents numerical results of turbulent transient simulations. The difficulty with such simulations is that any quantitative result should be established with ensemble averaging over a series of simulations with slightly different initial or boundary conditions, with some random noise for instance, to generate different samples of the same case. Here, we do not intend to present quantitative results in each case, but rather to identify the major trends, reproducible from a simulation to another. Proof of the grid convergence would also be extremely expensive, as ensemble averaging would be needed. Here we show that if the details of each simulation may differ, the major trends presented in the paper are reproducible.

We use case S75 to do so. For this case, we compare three calculations:

- run S75 used in the main text
- S75i: the same run as S75 but with different initial conditions: the final solution of run 1P75 is used as an initial condition for this run. The velocity in the jet region of the order of 1 cm/s in the initial condition (almost 2 orders of magnitude lower as the typical velocity at the mouth exit).
- S75fine: a run over a fine grid. The fine grid is the same as the main grid with each edge length halved (final grid 142 million elements).

First, it has to be stressed that the three jets are different, as shown with the jet angles: $\alpha = 0.207$ rad for S75 and $\alpha = 0.189$ rad for S75i and $\alpha = 0.233$ rad for S75fine: due to turbulence, the details of the jet growth differ from one simulation to another, even for the same grid. As a consequence, any data concerning a simulation case should only be considered as indicative, as differences of the order of 10% are shown in this example.

However, non-dimensional results and trends are perfectly reproducible, as shown in Fig. S2A: for all three cases, it is shown that after a few cycles, the jets length grows like $t^{1/2}$, but also that the prefactor of that scaling is the same whatever the initial conditions and the grid. Note that reproducibility is also shown between different runs (see Fig. 5E of the main text). As another example, grid independence of the results has been verified for C50, as shown in Fig. S2B. As a conclusion, results presented in the main text are reproducible and independent of the grid. However, numerical results specific to each case presented in the SI (and in particular in the right columns of Table S1) are only relative to one realization of the turbulent flows considered. If one is interested in specific results for each case, which is not the focus here, ensemble averaging should be performed.

Definition of the jet semi-angle. The semi-angle α reported in Table S1 is the semi-angle of a cone supposed to fit the jet development. Defining such a cone is actually not straightforward for statistical reasons: contrary to a steady round jet, the present jets are not statistically invariant with time nor in the azimuthal direction. In order not to be sensitive to small vortices, it was decided to define the fitting cone as the cone of radius 1.5 cm (the largest radius of the mouth opening) at $x = 0$ including 90% of the Lagrangian tracers injected. This percentage has been chosen to approximately fit the bulk development of the jet when looking at instantaneous fields of released particles. However, we have also verified that this definition is consistent with the

velocity field, as shown in Fig. S3. We note that the cones fit closely the jets, although the development is not identical for all cases. In particular, cases C75 and C100 seem to have a longer development region before a more conical growth. This is particularly visible for C100 and may explain why case C100 seems to be slightly different from the other cases in Fig. 5E. The use of an apparent origin, as classically done in turbulent jets, may improve this small discrepancy. Note finally that the value of the prefactor in the law of jet growth depends on the threshold used for defining the cone angle, or more generally on the way the cone angle is calculated.

Plume Reynolds numbers. The Reynolds number in the plume far from the inflow, which is a result of the calculations is also reported (last column of Table S1). Plume Reynolds number are estimated at $x = 1$ m, based on the local cycle-averaged axial velocity on the centerline and the radial extent of the jet. The radial extent of the jet is calculated over the plane $z = 0$ as the location at which axial velocity is 1/100th of the centerline velocity. Plume Reynolds numbers should be considered as indicative, as the cycle-averaged data is relatively noisy. However, Table S1 shows that plume Reynolds number are closer to the average Reynolds numbers than to the peak Reynolds numbers: far-field plume characteristics primarily depend on the averaged velocity rather than the details of the inflow signal.

Jet length and jet angles. Note that for a given mass flow rate, modulation of the in-flow signal (as in simulations P** and S**) is associated to shorter jets, but with a wider spread as shown by the semi-angle α reported in Table S1. The length is calculated only at the end of the cycles ($t = 4.0$ s, 8.0 s,...). Raw data of jet length along time are presented in Fig. S4. In the main text the same data is used in a non-dimensional plot (Fig. 5E).

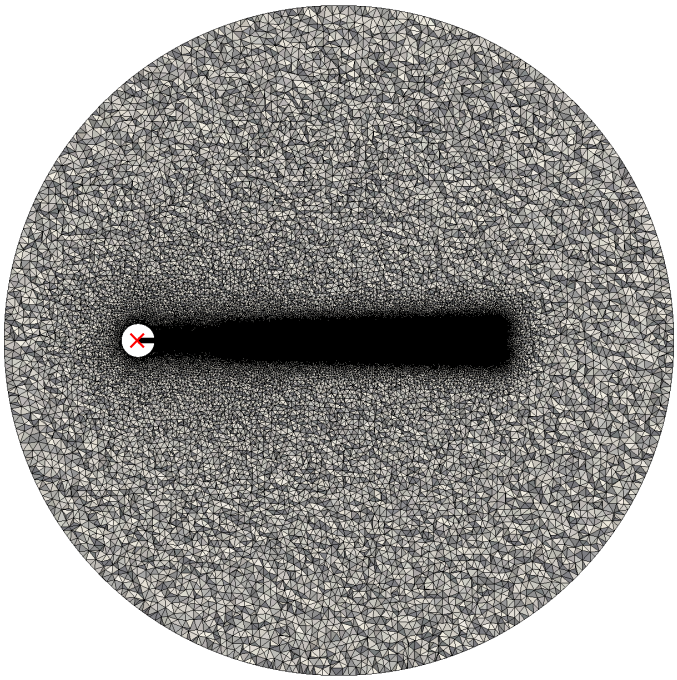

Fig. S1. 2D cutting plane ($z = 0$) of the computational domain with typical grid. The computational domain is a sphere of diameter 3 m. The red cross marks the in-flow, at $x = -0.075$ m. The head (small sphere) boundary conditions are solid walls. The external boundary conditions is a uniform velocity Dirichlet boundary condition that ensures mass conservation at all time.

Table S1. Table summarizing the characteristics of the numerical simulations. Columns left of the vertical bars are imposed parameters. The in-flow signals are presented in Fig. 4 of the main text. The Reynolds numbers Re of the last two columns before the vertical bar are calculated as $Re = 2aQ/\nu S$ with $a = 1.22$ cm the equivalent radius of the in-flow section, Q the flow rate (either the peak flow rate or the averaged flow rate during exhalation) and $S \approx 4.7$ cm^2 the surface area of the in-flow section. The last four columns are results of calculations (right of the vertical bar). Plume Reynolds number are calculated from the cycle-averaged axial velocity and the jet radial extent at $x = 1$ m. They are averaged over the last 4 cycles for each simulation.

Run ID	in-flow signal	Volume per breath (L)	Exhal. time (s)	Peak flow rate (L/s)	Average flow rate (L/s)	Peak Re	Average Re	Jet semi-angle α (rad)	Jet semi-angle α (deg)	Jet length (m) after 1 cycle	Plume Re
B50	Fig. 4A	0.50	2.4	0.274	0.208	949	722	0.224	12.6	0.70	857
C50	Fig. 4B	0.50	2.8	0.235	0.179	814	619	0.179	10.1	0.73	1014
C75	Fig. 4B	0.75	2.8	0.353	0.268	1222	928	0.171	9.7	0.82	1062
C100	Fig. 4B	1.00	2.8	0.470	0.357	1629	1238	0.203	11.5	0.96	1740
P50	Fig. 4C	0.50	2.8	0.612	0.179	2121	619	0.270	15.1	0.64	807
P75	Fig. 4C	0.75	2.8	0.918	0.268	3181	928	0.232	13.1	0.83	1137
P100	Fig. 4C	1.00	2.8	1.224	0.357	4242	1238	0.242	13.6	0.90	1660
S50	Fig. 4D	0.50	2.8	0.538	0.179	1864	619	0.207	11.7	0.54	788
S75	Fig. 4D	0.75	2.8	0.807	0.268	2797	928	0.207	11.7	0.60	1542
S100	Fig. 4D	1.00	2.8	1.076	0.357	3729	1238	0.230	13.0	0.68	1602
1P75	Fig. 4C if $t \leq 4$ s then 0	0.75	2.8	0.918	0.268	3181	928	0.232	13.1	0.83	-
1S50	Fig. 4D if $t \leq 4$ s then 0	0.50	2.8	0.538	0.179	1864	619	0.207	11.7	0.54	-

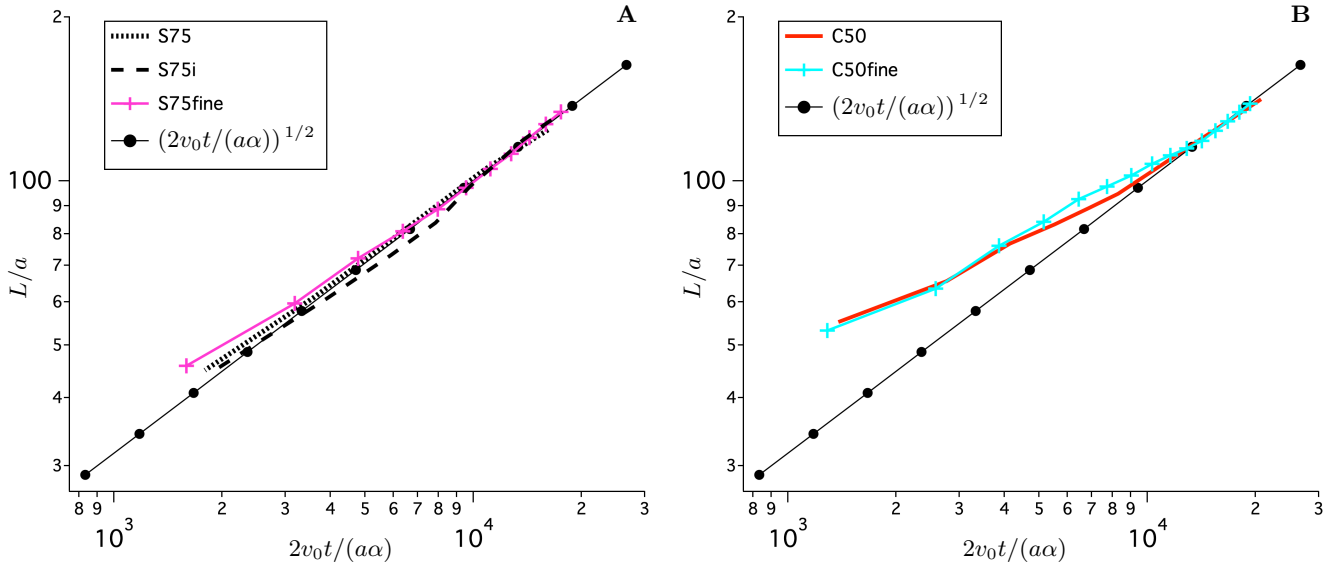

Fig. S2. Reproducibility and grid convergence: evolution of the non-dimensional jet length L/a as a function of $2v_0t/(a\alpha)$ (see Eq. 2 of the main text), with $a \approx 1.22$ cm the equivalent radius of the mouth exit and v_0 the average axial speed during exhalation. The power law is plotted as a guide for the eyes to assess the evolution of L with time. It is the same as in Fig. 5E. $\mathbf{A}$: case S75 with $v_0 \approx 0.568$ m/s in the three simulations reported. Results from simulation S75 are compared with the same simulation except for initial conditions, S75i. Results from a fine grid calculation are also reported: S75fine is performed in the exact same conditions as S75 albeit with a grid twice as fine in all directions. $\mathbf{B}$: case C50 with $v_0 \approx 0.379$ m/s in the two simulations reported. Results from simulation C50 are compared with C50fine, performed with a grid twice as fine in all directions.

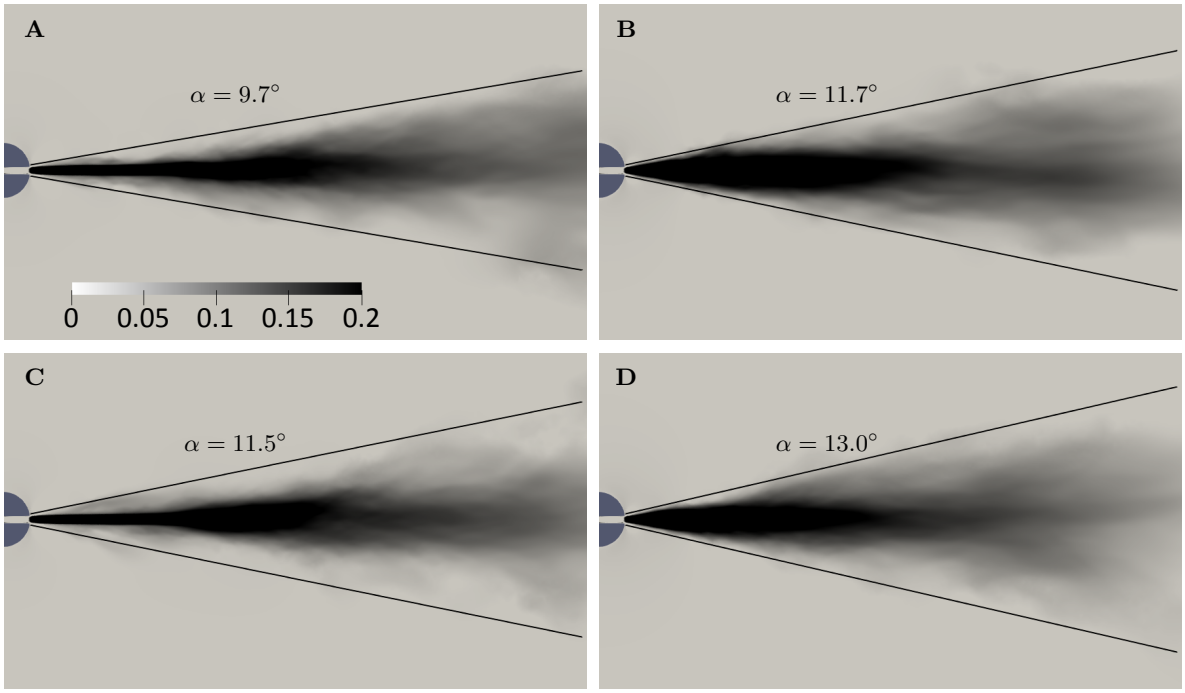

Fig. S3. Cycle-averaged axial velocity field for cases C75 (A), S75 (B), C100 (C) and S100 (D) over the 2D cutting plane $z = 0$. Solid lines mark the cone obtained using the definition with Lagrangian tracers (90% of the injected tracers are included in the cone. The lines stop at $x = 1.5$ m. Velocity is made non-dimensional using Q/S (see Table S1) as the characteristic velocity for each case. The color map is the same for all 4 cases. Cycle-averaged data are themselves averaged over the last 4 cycles of each run.

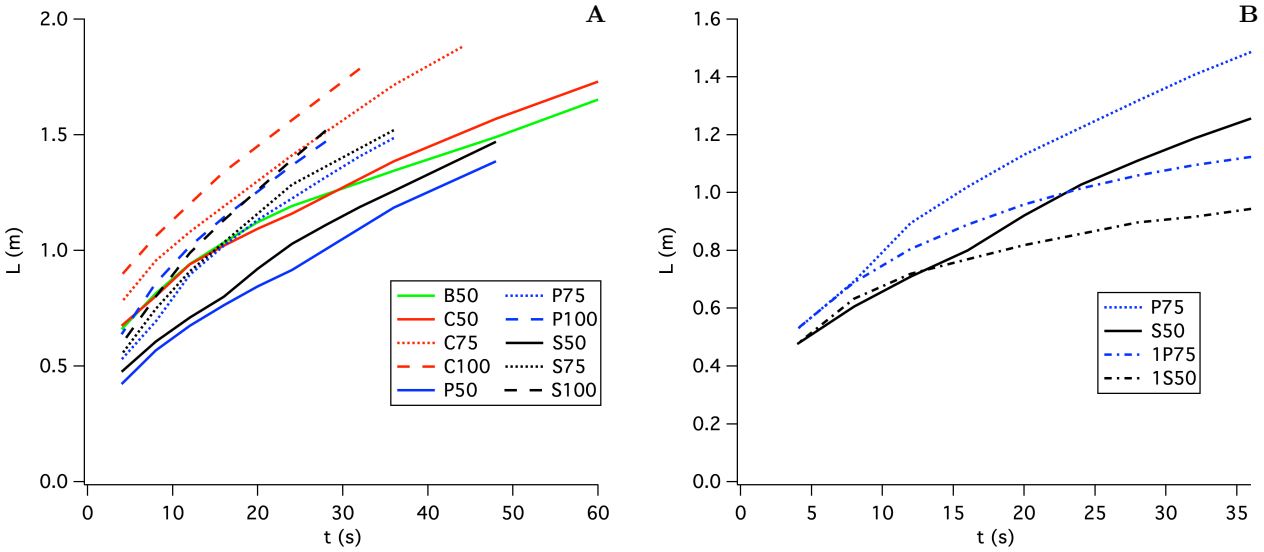

Fig. S4. Jet lengths $L(t)$ (based on the definition that 90% of injected tracers are upstream of the jet length L at time t) as a function of time for the different simulations listed in Table S1. $\mathbf{A}$. Multicycle simulations. $\mathbf{B}$. Comparison of 1 cycle simulations 1P75 and 1S50 with corresponding multicycle simulations P75 and S50.

Movie S1. (Upper panel) Bright field high-speed movie of a speaker calmly breathing twice with a slightly open mouth (1 cm × 2 cm), in direction of a laser sheet with a fog surrounding the head. (Lower Panel) Associated velocity magnitude field obtained by correlation image velocimetry.

Movie S2. (Upper panel) Bright field high-speed movie of a speaker blowing strongly in direction of a laser sheet with a fog surrounding the head. (Lower Panel) Associated velocity magnitude field obtained by correlation image velocimetry.

Movie S3. (Upper panel) Bright field high-speed movie of a speaker saying the sentence 'We will beat the corona virus' in direction of a laser sheet with a fog surrounding the head. (Lower Panel) Associated velocity magnitude field obtained by correlation image velocimetry.

Movie S4. (Upper panel) Bright field high-speed movie of a speaker saying the sentence 'Sing a song of six pence' in direction of a laser sheet with a fog surrounding the head. (Lower Panel) Associated velocity magnitude field obtained by correlation image velocimetry.

Movie S5. (Upper panel) Bright field high-speed movie of a speaker saying the sentence 'Peter Piper picked a peck' in direction of a laser sheet with a fog surrounding the head. (Middle Panel) Associated velocity magnitude field obtained by correlation image velocimetry. (Lower Panel) Associated vorticity field.

References

1. P Sagaut, *Large Eddy Simulation for Incompressible Flows: An Introduction.* (Springer Science & Business Media), (2006).
2. F Nicoud, H Baya Toda, O Cabrit, S Bose, J Lee, Using singular values to build a subgrid-scale model for large eddy simulations. *Phys Fluids* **23** (2011).
3. F Nicoud, C Chnafa, J Sigüenza, V Zmijanovic, S Mendez, Large-eddy simulation of turbulence in cardiovascular flows in *Biomedical Technology. Modeling, Experiments and Simulation*, Springer Series: Lecture Notes in Applied and Computational Mechanics, ed. TL P. Wriggers. pp. 147–167 (2018).
4. V Zmijanovic, S Mendez, V Moureau, F Nicoud, About the numerical robustness of biomedical benchmark cases: Interlaboratory FDA's idealized medical device. *Int J Num Meth Biomed Eng* **33**, e02789:1–17 (2017).
5. C Chnafa, S Mendez, F Nicoud, Image-based large-eddy simulation in a realistic left heart. *Comput. Fluids* **94**, 173–187 (2014).
6. V Moureau, P Domingo, L Vervisch, Design of a massively parallel CFD code for complex geometries. *Comp Rend Méc* **339**, 141–148 (2011).
7. V Moureau, P Domingo, L Vervisch, From large-eddy simulation to direct numerical simulation of a lean premixed swirl flame: Filtered laminar flame-PDF modelling. *Comb Flame* **158**, 1340–1357 (2011).
8. A Chorin, Numerical solution of the Navier–Stokes equations. *Math Comp* **22**, 745–762 (1968).
9. J Kim, P Moin, Application of a fractional-step method to incompressible Navier-Stokes equations. *J Comp Phys* **59**, 308–323 (1985).
10. M Kraushaar, Ph.D. thesis (CERFACS, Toulouse, France) (2011).
11. M Malandain, N Maheu, V Moureau, Optimization of the deflated conjugate gradient algorithm for the solving of elliptic equations on massively parallel machines. *J Comp Phys* **238**, 32–47 (2013).
12. C Geuzaine, JF Remacle, Gmsh: A 3-d finite element mesh generator with built-in pre-and post-processing facilities. *Int J Num Meth Eng* **79**, 1309–1331 (2009).